TU/e EINDHOVEN UNIVERSITY OF TECHNOLOGY

Kinodynamic Generation of Wafer Scanners Trajectories Used in Semiconductor Manufacturing

Citation for published version (APA):
Al-Rawashdeh, Y. M., Al Janaideh, M., & Heertjes, M. F. (2023). Kinodynamic Generation of Wafer Scanners Trajectories Used in Semiconductor Manufacturing. *IEEE Transactions on Automation Science and Engineering*, *20*(1), 718-732. https://doi.org/10.1109/TASE.2022.3196318

Document license:
TAVERNE

DOI:
10.1109/TASE.2022.3196318

Document status and date:
Published: 01/01/2023

Document Version:
Publisher's PDF, also known as Version of Record (includes final page, issue and volume numbers)

Please check the document version of this publication:

• A submitted manuscript is the version of the article upon submission and before peer-review. There can be important differences between the submitted version and the official published version of record. People interested in the research are advised to contact the author for the final version of the publication, or visit the DOI to the publisher's website.
• The final author version and the galley proof are versions of the publication after peer review.
• The final published version features the final layout of the paper including the volume, issue and page numbers.

Link to publication

General rights
Copyright and moral rights for the publications made accessible in the public portal are retained by the authors and/or other copyright owners and it is a condition of accessing publications that users recognise and abide by the legal requirements associated with these rights.

• Users may download and print one copy of any publication from the public portal for the purpose of private study or research.
• You may not further distribute the material or use it for any profit-making activity or commercial gain
• You may freely distribute the URL identifying the publication in the public portal.

If the publication is distributed under the terms of Article 25fa of the Dutch Copyright Act, indicated by the "Taverne" license above, please follow below link for the End User Agreement:

www.tue.nl/taverne

Take down policy
If you believe that this document breaches copyright please contact us at:

openaccess@tue.nl

providing details and we will investigate your claim.

Download date: 04. Oct. 2023

Kinodynamic Generation of Wafer Scanners Trajectories Used in Semiconductor Manufacturing

Yazan M. Al-Rawashdeh, Mohammad Al Janaideh, and Marcel F. Heertjes

***Abstract*— The operation time of an *ideal* reliable wafer scanner model is defined at the die level where the actual exposure process takes place as the time unit per die, or at the wafer substrate level as the time unit per wafer substrate. Therefore, the machine throughput is given as the reciprocal of the operation time. The involved motion profiles of a machine, namely the step-and-scan trajectories, function as the heartbeats that drive its multidisciplinary elements, which suggests that a multidisciplinary design optimization should be involved when such profiles are selected or designed. This is also true when considering the traverse motion profiles among rows and columns within the wafer substrate. The step-and-scan trajectories affect the machine throughput, performance, and die yield. The effects of tracking such profiles appear as structural vibration, tracking errors, and thermal loading at various machine elements such as the actuators, the reticle, the wafer, and the projection elements specifically when the exposure high-energy duration and frequency are not taken into consideration while designing the reference motion. From the dynamics perspective, having a reference motion with nonzero and bounded higher-order derivatives is recommended since it enhances the tracking performance of the machine, however, its ability to increase the operation time is usually overlooked. In an attempt to understand such effects, we present a case study that outlines the aforementioned aspects using three step-and-scan profiles of mainly 3^{rd}-order. Taking the dynamics of the driven stage into consideration through input shaping, both the step-and-scan and traverse motion profiles are analyzed. We provide analytical expressions that can be used to generate both types of motion profiles on the fly without additional optimization. A simulation example of a simplified wafer scanner machine shows the usefulness of the proposed framework.**

***Note to Practitioners*—Choosing the most suitable operating conditions of a lithography machine is challenging. These conditions affect machine productivity, profit margin, and maintenance. In this paper, we reveal the relation between the selection of operating conditions based on several decision variables- and the kinodynamic step-and-scan trajectory generation based on specific machine parameters and clients' requirements. Being chart-based, the selection process of an operating point can be less practical at some points. However, using appropriate curve fitting tools, the information provided in the optimal operating charts can be put into suboptimal closed-form expressions that facilitate the selection process. Therefore, the designed trajectories parameters can be easily saved in lookup tables for ease of evaluation and future use. This helps in accommodating changes in the operation plans and flexible manufacturing systems. Also, starting with a given set of machine parameters, it is possible to calculate the optimal machine operating point when the input shaping technique is used, as illustrated in this paper.**

***Index Terms*— Trajectories, input shaping, throughput, lithography, operating point, operating charts, step-and-scan, traverse motion, analytical expressions.**

Manuscript received 21 January 2022; accepted 23 March 2022. Date of publication 22 September 2022; date of current version 6 January 2023. This article was recommended for publication by Associate Editor C.-Y. Lee and Editor F.-T. Cheng upon evaluation of the reviewers' comments. This work was supported in part by the Natural Sciences and Engineering Research Council of Canada (NSERC) and in part by Memorial University. *(Corresponding author: Mohammad Al Janaideh.)*

Yazan M. Al-Rawashdeh and Mohammad Al Janaideh are with the Department of Mechanical Engineering, Memorial University, St. John's, NL A1B 3X5, Canada (e-mail: yalrawashdeh@mun.ca; maljanaideh@mun.ca).

Marcel F. Heertjes is with ASML, 5504 DR Veldhoven, The Netherlands, and also with the Department of Mechanical Engineering, Eindhoven University of Technology, 5612 AZ Eindhoven, The Netherlands (e-mail: marcel.heertjes@asml.com).

Color versions of one or more figures in this article are available at https://doi.org/10.1109/TASE.2022.3196318.

Digital Object Identifier 10.1109/TASE.2022.3196318

Number Sets

$\mathbb{R}$	Real numbers
$\mathbb{C}$	Complex numbers

Constants

$$j = \sqrt{-1} \in \mathbb{C}$$

Real Parameters

$a, a_{\{\cdot\}}, a_{\{\cdot\}}^{max}$	Maximum acceleration values	ms^{-2}
$a_{\{\cdot\}}(t)$	Acceleration profile	ms^{-2}
$v(t)$	Velocity profile	ms^{-1}
$p(t)$	Position profile	m
J_{scan}, J_{step}	Maximum {scan,step} jerk value	ms^{-3}
$T_1 > 0$	De/acceleration time interval	s
$T_2 \geq 0$	Constant acceleration time interval	s
$T_3 \geq 0$	Idle time interval s	
$T_w \geq 0$	Time between scan and step motions	s
$T_s, T_E \geq 0$	Preparation and exposure times	s
$P_{T_s} \geq 0$	Preparation distance	m
$D, d \geq 0$	Constant {scan,step} speed time interval	s
$s,\ \tilde{s} > 0$	Time scaling factors	
$s_{scan} > 0$	Scanning time scaling factor	
$s_{step} > 0$	Stepping time scaling factor	
$P_{scan} \geq 0$	Scanning phase pitch size	m
$P > 0$	Scanning distance	m
$V_{\{\cdot\}} > 0$	{Scan,step} velocity	ms^{-1}
$P_{step} \geq 0$	Stepping phase pitch size	m
$\mathcal{F}\{\cdot\}$	Fourier transform	

1545-5955 © 2022 IEEE. Personal use is permitted, but republication/redistribution requires IEEE permission.
See https://www.ieee.org/publications/rights/index.html for more information.

Authorized licensed use limited to: Eindhoven University of Technology. Downloaded on June 26,2023 at 08:45:42 UTC from IEEE Xplore. Restrictions apply.

t	Time	s
f	Frequency	Hz
$\omega, \tilde{\omega}_{\{\cdot\}}^{\{\cdot\}}, \omega_{\{\cdot\}}^{\{\cdot\}}$	Radial frequency	rads^{-1}
PR_p	Motion profile productivity ratio	%
PR_M	Machine productivity ratio	%
OP	Operation time	s
$L > 0$	Die length	m
$W > 0$	Die width	m
$H > 0$	Slit height	m
$\epsilon_v, \epsilon_h > 0$	Width of {vertical, horizontal} scribe lanes	m
$N \geq 1$	Number of dies	
$x_{off}, y_{off} \geq 0$	Idle time for $\{x, y\}$ motion axes	s
$T_L, T_U \geq 0$	Wafer substrate {loading, unloading} time	s
$T_A \geq 0$	Wafer substrate alignment time	s
$T_P \geq 0$	Wafer substrate total processing time.	

I. Introduction

LITHOGRAPHY machines- or more specifically optical lithography wafer scanner machines are complex mechatronics systems where energy flows back and forth multidisciplinary domains. The machine synchronizes motion and light to print replicas of integrated circuits images onto a silicon disk, known as *wafer* [1]. The integrated circuit pattern (the mask) exists on a quartz plate, called *mask or reticle* [2], being part of the reticle stage motion control system. In these machines, a step-and-scan profile is adopted, where a small rectangular area of the wafer, known as *die*, is exposed under constant velocity (scanning process) during which the wafer is moving- by the wafer stage- in the direction opposite to the reticle which is moved by the reticle stage. The reticle stage acceleration may reach $180\,\text{m/s}^2$ when the actual exposure process is not taking place. Once the projection of a single die is done, the wafer stage moves the wafer to the next die location (stepping process) where acceleration values of $45\,\text{m/s}^2$ are possible [3], [4]. Scanning is done with a constant velocity, while stepping is done with maximum acceleration/deceleration of the stage as to reduce the machine operation time, and therefore tracking errors and vibration are induced [5]. To reduce the tracking errors, nonzero and bounded higher-order time derivatives can be used in the design process to increase the order of the reference motion, and this is usually accompanied by feedforward controllers [2], [6]. It is possible that the operation time of the new higher-order reference motion increases to accommodate the new terms, and this may reduce the throughput when kinematical constraints are applied and the final position is held constant, i.e. point-to-point applications. This is usually overlooked, or implicitly stated [6], [7]. A more elaborate design process should take place when thermal [8], optical [9], kinematical, dynamical performance- including saturation limits at the actuators- and temporal constraints are introduced.

Having thermal models of various parts of the lithography machine helps in understanding the effect of the reference motion on such parts [10]. Tracking the repetitive reference motion heats up the actuators responsible for the spatial motion [10]. Having thermo-electro-mechanical models of the actuators and their cooling systems definitely helps in choosing the kinematical constraints to be used in the reference motion design process [11]. The same rationale is true about the optical elements involved; since the exposure process is synchronized with the spatial motion [12], [13]. Finally, being a part of a production line, the wafer scanner has to meet minimum throughput requirements to ensure certain levels of production rates.

Usually, the improvement of motion control system performance is achieved by using higher-order motion profiles, especially under feedforward control. Higher-order motion profiles have a lower power spectrum at higher frequencies, resulting in a reduced positioning error at high frequency, and therefore the feedback controller becomes more effective [6]. Also, such profiles are physically more realizable; since it is impossible for most power amplifiers to produce a step-like change in force [6].

Triggering the driven motion stages lightly-damped modes by the inertial forces can cause structural vibrations. These vibrations can be reduced by the motion control itself [14], active vibration suppression or isolation techniques [15], input shaping [16]–[18] and filtering techniques [19]. Avoid triggering these modes in the first place seems reasonable [14], and therefore it is recommended to look into the making of the reference trajectories before applying any other methods.

Considering the previous points, the main contributions of the current study are as follows:

1) By upgrading a 2^{nd}-order to a 3^{rd}-order motion profile, we analyze the operational cost associated with increasing the motion profile order, and jointly study the step-and-scan a/symmetric trajectory generation at the die level, and provide three distinct 3^{rd}-order *symmetric* motion profiles.
2) Provide analytical expressions that can be used to study, analyze and optimize the proposed motion profiles. This enables selecting the best operating point when multidisciplinary constraints are imposed using the optimal operating charts resulting from the kinematical optimization problem.
3) By working at the wafer substrate level, the extrapolation of the planner traverse motion between rows and columns is given in an easy to manipulate analytical form.
4) Provide relations between closed-loop dynamical properties and kinematical motion profile quantities under input shaping at the selected operating point.

Following the same rationale as in [20] and by assuming the machine is reliable [21], we present a case study that gives a glimpse of the complexity of the design process when *mainly* kinematical and temporal operational constraints are imposed. Once the operating charts are generated, a suitable operating point is selected and used under input shaping to tune the closed-loop controllers of a simplified wafer scanner

Authorized licensed use limited to: Eindhoven University of Technology. Downloaded on June 26,2023 at 08:45:42 UTC from IEEE Xplore. Restrictions apply.

machine. Note that using the closed-loop dynamics to select the best operating point from the operating charts is also possible, and will be investigated separately. In this study, three symmetric 3^{rd}-order step-and-scan profiles to guide the motion of the wafer scanner during the step-and-scan motion are presented in Section II, and through an optimization setting we show how do they relate- *specifically*- to the 2^{nd}-order profile in [2]. Kinodynamic trajectory generation is handled in Section III where both the step-and-scan and traverse trajectories are integrated with the machine dynamics and the used closed-loop controllers. The operating charts, the operating point selection, and the resulting trajectory-machine setup responses are provided in Section IV. Final remarks are given in Section V.

II. Reference Trajectories

A generalized *switched-polynomial* positioning motion profile of q^{th}-order that can be used to design the step and the scan trajectories in wafer scanners $\forall t \in I_l$ is given as

$$p(t) = \sum_{i=0}^{q} \alpha_i^l \, t^i = \alpha_0^l + \alpha_1^l \, t + \alpha_2^l \, t^2 + \cdots + \alpha_q^l \, t^q \qquad (1)$$

where t denotes the time, and the *switched* coefficients $\alpha_i^l, i = 0, 1, 2, \cdots, q$ in the l^{th} interval I_l with $l = 1, 2, \cdots, 2^q - 1$, and q denotes the switched-polynomial order defined as

Definition 1: In a switched-polynomial motion profile, the order q is given as the largest degree (or order) of the polynomials in all intervals.

In this study, we focus on the case where $q = 3$ for which the associated symbolic values of the switched coefficients- *when $t_0 = 0$, and with zero initial velocity and acceleration*- are given in APPENDIX A. These coefficients are functions of the *maximum acceleration value* denoted by (a) and given in $\mathrm{m/s^2}$, the length of varying acceleration and deceleration time intervals (T_1), the length of constant acceleration time intervals (T_2), the length of the constant speed time interval (D) all given in *seconds*, and a scaling factor $(s > 0 \in \{s_{scan}, s_{step}\})$. The used 3^{rd}-order motion profile is depicted in Fig. 1. Moreover, we have the following terminologies

Definition 2: In the 3^{rd}-order motion profile depicted in Fig. 1, if $|a_1| = |a_2|$, then the profile is deemed *symmetric*, otherwise it is *asymmetric*, and the associated jerk profile follows.

Definition 3: In this study, a higher-order motion profile has an order greater than 2, i.e., $q > 2$.

In [2], a 2^{nd}*-order* profile with constant acceleration and infinite jerk values was used in an example. Adopting [2] as a case study, we will use the 3^{nd}-order profile given by (1) to approximate this 2^{nd}-order profile such that a finite maximum jerk value is obtained, and also to investigate the effect of the motion profile order on various operational quantities and performances. To that end, we fix T_1 and T_2 and let s and D to vary independently. This turned out to be useful when the total time of the motion profile is minimized. However, other choices are still valid.

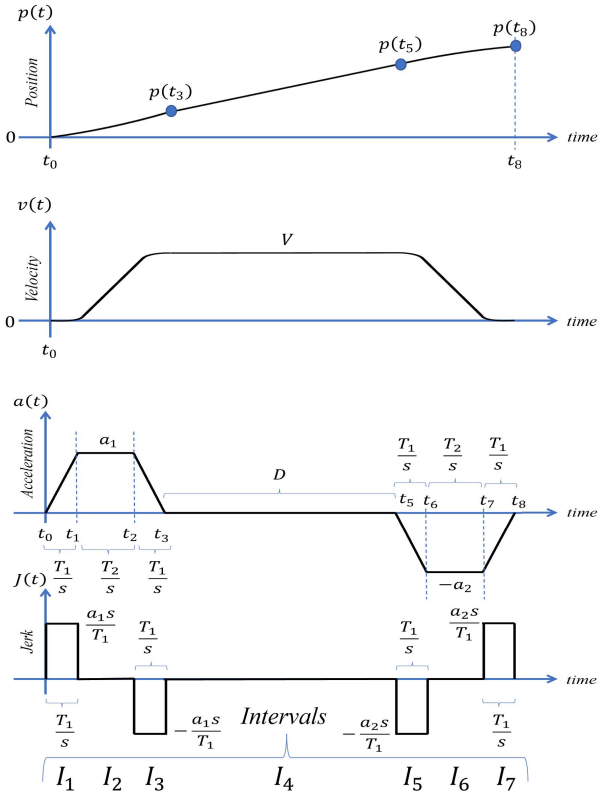

Fig. 1. The generalized symmetric 3^{rd}-order motion profile used in this study to present the step and the scan profiles.

Starting at the symmetric jerk profile depicted in Fig. 1, the Fourier transform of $p(t), \forall t \in [t_0, t_8]$ is given as

$$\begin{aligned}\mathcal{F}\{p(t)\} &= A \, \sin\left(\pi \, f \, \frac{T_1}{s}\right) \sin\left(\pi \, f \left(\frac{T_1 + T_2}{s}\right)\right) \\ &\quad \times \sin\left(\pi \, f \left(\frac{2\,T_1 + T_2}{s} + D\right)\right) \\ A &= \frac{a\,s}{2\,j\,(\pi\,f)^4\,T_1} \exp\left(-j\pi \, f \left(\frac{4\,T_1 + 2\,T_2}{s} + D\right)\right)\end{aligned} \qquad (2)$$

Similarly, the power spectrum of the asymmetric jerk profile $J(t)$ depicted in Fig. 2 is given as

$$\begin{aligned}\mathcal{F}\{J(t)\} &= B \, \sin\left(\pi \, f \, \frac{T_1}{s}\right) \sin\left(\pi \, f \left(\frac{T_1 + T_2}{s}\right)\right) \\ &\quad + C \, \sin\left(\pi \, f \, \frac{T_3}{\bar{s}}\right) \sin\left(\pi \, f \left(\frac{T_3 + T_4}{\bar{s}}\right)\right) \\ B &= \frac{-2\,a_1\,s}{j\pi\,f\,T_1} \exp\left(-j\pi \, f \left(\frac{2\,T_1 + T_2}{s}\right)\right) \\ C &= \frac{2\,a_2\,\bar{s}}{j\pi\,f\,T_3} \\ &\quad \times \exp\left(-2j\pi \, f \, D\right) \exp\left(-3j\pi \, f \left(\frac{2\,T_3 + T_4}{\bar{s}}\right)\right)\end{aligned} \qquad (3)$$

Note that in this study, we mainly focus on *symmetric* 3^{rd}-order motion profiles.

Authorized licensed use limited to: Eindhoven University of Technology. Downloaded on June 26,2023 at 08:45:42 UTC from IEEE Xplore. Restrictions apply.

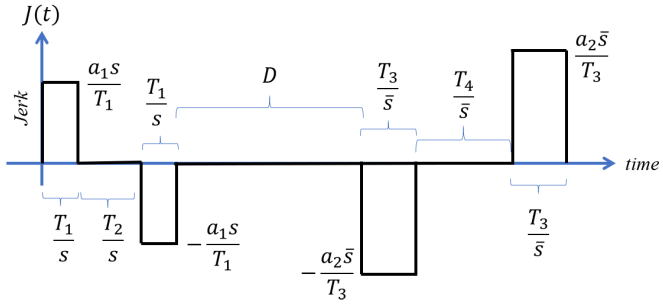

Fig. 2. A generalized asymmetric 3^{rd}-order motion profile.

Remark 1: Interestingly, (2) can be used to *design* and investigate the frequency contents in the developed symmetric trajectory. For example, under input shaping where specific frequencies in the power spectrum of the reference do not have any frequency content whatsoever, we could tune the ratio $\frac{T_1}{s}$, i.e., maximum acceleration over maximum jerk, in regard to the first plant resonances. Alternatively, we may tune the ratio $\frac{T_1+T_2}{s}$, i.e., maximum velocity over maximum acceleration, but this is often less preferred. This is the key mechatronic usage currently in wafer scanners. Note that going from 2^{nd}-order to 3^{rd}-order profile means 20 $dB/decade$ less excitation/power at higher frequencies. A detailed utilization of (2) and its relation with an input shaping control technique are studied in Section III. For an asymmetric profile, (3) can be used instead.

A. The Step-and-Scan Trajectories Based on the Generalized Motion Profile

Targeting to wafer scanners, (1) is used to design three step-and-scan trajectories that differ in the way the x-motion, i.e., stepping, and the y-motion, i.e., scanning, relate to each other. Besides other features, each profile may have a different throughput value at any given machine operating conditions as well. From a Kinematics point of view, both the step and the scan trajectories can be designed as scaled versions of the trajectory given in (1). By integrating the jerk profile depicted in Fig. 1 from I_1 to I_7 three times, the *scanning phase pitch size* (P_{scan}) depicted in Fig. 3 is given as

$$\begin{aligned} P_{scan} &= p(t_8) = \frac{\alpha_1^4}{s_{scan}}\left(2\,T_1 + T_2 + D\,s_{scan}\right) \\ &= \frac{a_{scan}^{max}\,(T_1+T_2)\,(2\,T_1+T_2+D\,s_{scan})}{s_{scan}^2} \end{aligned} \tag{4}$$

where $s_{scan} > 0$ is the scaling factor used in the scanning motion. For the asymmetric motion profile captured in Fig. 2, the resulting P_{scan} is given as

$$\begin{aligned} P_{scan} = &\left\{\frac{(T_1+T_2)(2\,T_3+T_4+D\,\bar{s})}{s\,\bar{s}}\right\} a_1 \\ &+ \left\{\frac{2\,T_1^2+3\,T_1\,T_2+T_2^2}{2\,s^2}\right\} a_1 \\ &- \left\{\frac{2\,T_3^2+3\,T_3\,T_4+T_4^2}{2\,\bar{s}^2}\right\} a_2 \end{aligned} \tag{5}$$

where $\bar{s} > 0$ is another scaling factor. Note that when $T_3 = T_1, T_4 = T_2, a_2 = a_1 = a_{scan}^{max}$ and $\bar{s} = s = s_{scan}$, then the motion profile becomes symmetric and (4) is obtained. Likewise, the *stepping phase pitch size* (P_{step}) depicted in Fig. 3 under (1) is given as

$$\begin{aligned} P_{step} &= W + \epsilon_v = \frac{\alpha_1^4}{s_{step}}\left(2\,T_1 + T_2 + d\,s_{step}\right) \\ &= \frac{a_{step}^{max}\,(T_1+T_2)\left(2\,T_1+T_2+d\,s_{step}\right)}{s_{step}^2} \end{aligned} \tag{6}$$

where $s_{step} > 0$ is the scaling factor used in the stepping motion, W is the die width and ϵ_v is the width of the scribe lane separating adjacent dies vertically, both given in *meters*. Using d instead of D in (5) results in P_{step} given for the asymmetric profile depicted in Fig. 2.

From Fig. 3, it is clear that P_{scan} is a function of the fixed machine parameter, i.e., the *slit height* (H), the *die length* (L) to be produced, the *preparation distance* P_{T_s}- in which the tracking errors are allowed to drop to acceptable levels [2]- and the acceleration/deceleration *overrun distance* $p(t_3)$. The latter two distances constitute the non-productive portion of the scanning trajectory, and therefore should be minimized. The distance $p(t_3)$ is given as

$$p(t_3) = -\alpha_0^4 \tag{7}$$

and the *scanning distance* (P) is given as

$$P \triangleq p(t_5) - p(t_3) = P_{T_s} + L + H \tag{8}$$

where P_{T_s} is given as

$$P_{T_s} = \frac{a_{scan}^{max}\,(T_1+T_2)\,D}{s_{scan}} - (L+H) \tag{9}$$

Remark 2: Note that the stepping motion is a point-to-point motion while the scanning motion needs only to travel the desired scanning distance P with a desired scanning speed.

The constant *scanning speed* during the exposure process (V_{scan}) for the symmetric motion profile is given as

$$V_{scan} = \alpha_1^4 \tag{10}$$

which is also valid for the asymmetric motion profile with $a_1 = a_{scan}^{max}$ and $s = s_{scan}$. The *preparation time* (T_s) available under given machine operating conditions is given as

$$T_s^{min} \le T_s = \frac{P_{T_s}}{V_{scan}} \le T_s^{max} \rightarrow V_{scan} \ge \frac{L+H}{D - T_s^{min}} \tag{11}$$

where T_s^{min} is the minimum preparation time that is needed to prepare for the exposure process, and/or as a settling time to the residual tracking errors, and T_s^{max} is its maximum value. Therefore, when designing the tracking controllers, T_s should be considered, may be as the settling time, where any needed bounds can be introduced to the motion profile design process.

The *exposure time* (T_E) is the *actual* time during which the exposure process is taking place. It is given as

$$\begin{aligned} T_E^{min} \le T_E &\triangleq t_{off} - t_{on} = D - T_s \\ &= \frac{s_{scan}\,(L+H)}{a_{scan}^{max}\,(T_1+T_2)} = \frac{s_{scan}^2\,(L+H)}{J_{scan}\,T_1\,(T_1+T_2)} \le T_E^{max} \end{aligned} \tag{12}$$

where J_{scan} is the maximum jerk value of the scan profile, T_E^{max} is the maximum allowed exposure time which can be determined based on the thermal models of the optics system and the wafer substrate, and T_E^{min} is its minimum value.

Authorized licensed use limited to: Eindhoven University of Technology. Downloaded on June 26,2023 at 08:45:42 UTC from IEEE Xplore. Restrictions apply.

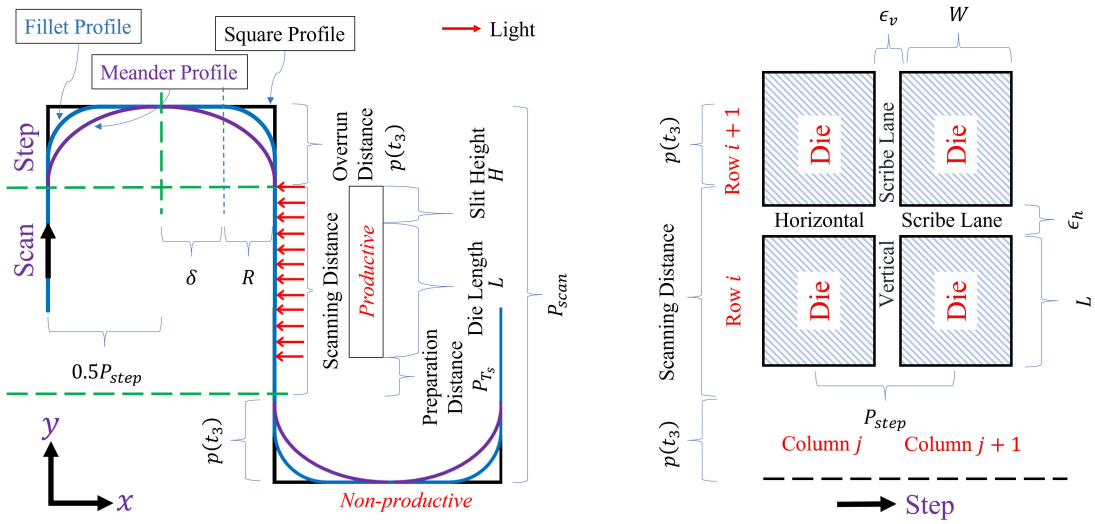

Fig. 3. The step-and-scan x-y trajectories using square, (shifted) meander and fillet motion profiles.

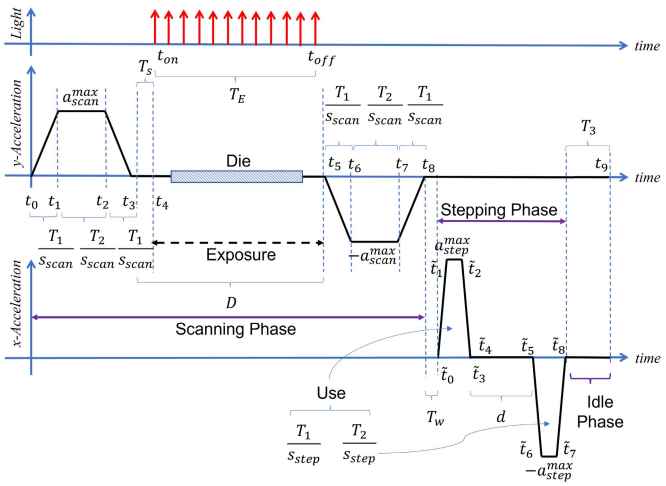

Fig. 4. The proposed symmetric square acceleration trajectories along with the light source activation timing.

Interestingly, (12) reveals the relation between any available thermal models, and the kinematical constraints that are used to design or select the reference motion profiles. Moreover, it shows the trade-off between the thermal performance of the machine, its tracking performance, and the attainable throughput. For example, increasing J_{scan} reduces $T_E \geq T_E^{min}$, and consequently the thermal effects, but it may cause a degradation in the tracking performance. Therefore, any available thermal models should be considered in the multi-disciplinary design process of the reference motion profiles. Note that the bounds on both T_s and T_E can affect also the stepping motion profile based on the realization of the step-and-scan trajectories.

1) The Square Profile: Recalling Fig. 4, this symmetric motion profile decouples the desired motion during the stepping, i.e., in the x-direction, and the scanning phase, i.e., in the y-direction, during any step-and-scan cycle. Also, it can increase the machine operation time unless the non-productive phase of motion dominated by the stepping phase is reduced, which may require increasing the stepping acceleration (a_{step}^{max}). Increasing a_{step}^{max} can reduce the machine performance by increasing the tracking errors and induced vibration. A square stepping trajectory with a *suitable* s_{step} value and $d = 0$ *may* help in mitigating such effects. Therefore, a trade-off between throughput and performance should be considered. Also, the parameter $T_w \geq 0$ governs the separation between the stepping and the scanning trajectories, while the idle phase governed by the parameter $T_3 \geq 0$ separates the step-and-scan cycles. Both T_3 and T_w can be independently optimized or set by the operator.

2) The Meander Profile: Recalling Fig. 5, to increase the productivity of the symmetric meander profile during any step-and-scan cycle, the stepping phase is equally split over the non-productive scanning motion. However, when the x-y motion of driven positioning stage is realized independently, i.e., using decoupled actuators like H-configuration [2], then the y-axis actuator may get overheated unless $T_3 \neq 0$. When actuators are coupled under some configurations, the actuators power gets distributed between y and x motions, which increases the drawbacks associated with the square profile. According to Fig. 3, the pointy step-and-scan meander profile in the x-y plane may introduce tracking problems when the machine dynamics are involved. Similar to the square profile, (4) through (12) except (6) are still valid. For P_{step} under the meander profile, it is half of that given in (6). This reduces the a_{step}^{max} values used, especially when $d = 0$ which gives rise to an inflection point at $t = \frac{2T_1+T_2}{2s_{scan}}$. At the inflection point, the stepping profile curvature will change its sign.

Note that in the meander profile, both the step and the scan trajectories must be designed concurrently as

$$\frac{2\,(2T_1 + T_2)}{s_{step}} + d = \frac{(2T_1 + T_2)}{s_{scan}} \tag{13}$$

3) The Fillet Profile: As depicted in Fig. 6, the symmetric fillet profile splits the stepping phase between successive cycles, which appears as a flat region in the x-y plane with constant stepping velocity in the x-direction during two step-and-scan cycles once compared to the meander profile. The fillet profile also provides rounded edges once compared to

Authorized licensed use limited to: Eindhoven University of Technology. Downloaded on June 26,2023 at 08:45:42 UTC from IEEE Xplore. Restrictions apply.

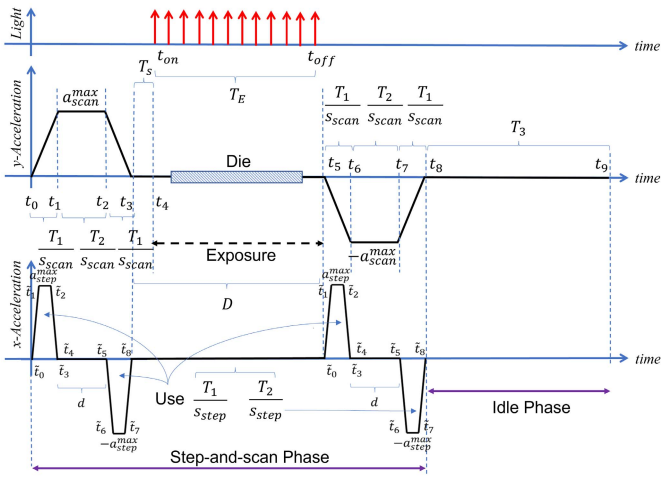

Fig. 5. The proposed symmetric meander acceleration trajectories along with the light source activation timing.

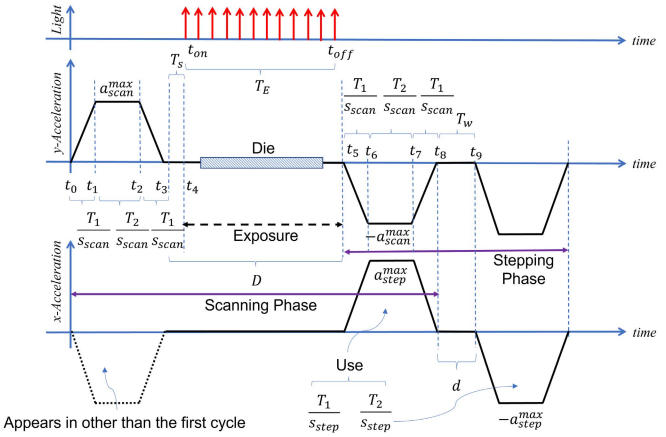

Fig. 6. The proposed symmetric fillet acceleration trajectories along with the light source activation timing. When $T_w = 0$, then a meander-like profile can be obtained from the fillet profile. Therefore, the meander profile can be considered as a subset of the fillet profile when $d \equiv T_w = 0$.

the square profile, and therefore better tracking performance is *expected* when the machine dynamics are involved. Similar to the square profile, (4) through (12) are still valid. By matching Fig. 6 and Fig. 3, it is clear that

$$s_{scan} = s_{step}, \quad R \triangleq p(t_3) = \frac{P_{step}}{m}$$
$$\delta = \frac{a^{max}_{step}\,(T_1 + T_2)\,T_w}{2\,s_{step}} = \frac{P_{step}}{n} \tag{14}$$

where (7) and (8) were written using the stepping phase variables, and both $(\infty \gg m, n > 2) \in \mathbb{R}$ determines how much roundness and flatness are in the fillet profile, respectively. Also, from Fig. 3, we may write

$$P_{step} = 2R + 2\delta = 2\left(\frac{n+m}{n\,m}\right)P_{step}$$
$$2 = \frac{n\,m}{n+m} \rightarrow m = \frac{2\,n}{n-2}, \quad n = \frac{2\,m}{m-2} \tag{15}$$

If $\delta \rightarrow 0$ or $T_w \rightarrow 0$, then $n \rightarrow \infty$, and $m \rightarrow 2$. Consequently, there is less flatness involved in the profile. Therefore, a meander-like profile emerges, however, with possibly higher values of a^{max}_{step}. Therefore, the meander profile can be considered as a subset of the fillet profile when $d \equiv T_w = 0$. Note that retrieving a square-like profile from the fillet profile is practically unattainable.

Remark 3: Using asymmetric motion profiles depicted in Fig. 2 allows introducing more steep, i.e. aggressive, profiles during slow down (after scanning), and least steep, i.e. friendly, profiles prior to scanning [22]. This is possible by adjusting the parameters given in (5), and therefore the operation time can be reduced while maintaining desired performance during the exposure phase. This will be investigated in detail in future work.

B. Approximating 2^{nd}-Order Motion Profiles Using 3^{rd}-Order Motion Profiles

The benefit of using 3^{rd}-order trajectory profiles to approximate the 2^{nd}-order trajectory profile used in [2] is immediately evident from the finite jerk values obtained. This is usually done to limit the jerk values *to suite typical positioning stages in lab settings* with probably acceleration levels below than $20\,\mathrm{m/s^2}$. In an industrial setting, typical jerk values may exceed $10000\,\mathrm{m/s^3}$, with acceleration levels exceeding $100\,\mathrm{m/s^2}$. In this study, we desire $J_{scan} = 6\,\alpha_3^1 \leq 1600$ as the maximum jerk value. In addition to the finite jerk values, rich frequency contents of the higher-order motion profiles make it possible to include certain frequencies under input shaping, as discussed later. These frequencies could be motion-related or vibration-related. In this subsection, we would like to show how such an approximation can be made possible, and what are the advantages and costs associated with it.

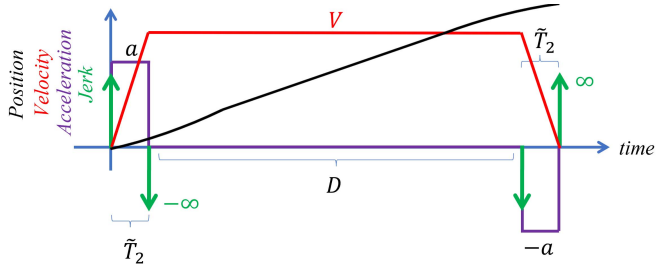

Fig. 7. The 2^{nd}-order motion profile used in [2]. Not to *scale*.

Fig. 7 shows the 2^{nd}-order acceleration profile used in [2] with constant scanning speed of $0.25\,\mathrm{m/s}$ and maximum acceleration $a = 10\,\mathrm{m/s^2}$. This speed is equal to the area under the first rectangle in this acceleration profile. Therefore, the constant acceleration time ($\tilde{T}_2$) equals $0.25/10 = 0.025\,\mathrm{s}$. Also, a total scanning length ($\tilde{P}$) of 54.5 mm was reported. So, the scanning time $D = 0.0545/0.25 = 0.218\,\mathrm{s}$, and the calculated scanning phase pitch size ($\tilde{P}_{scan}$) equals 0.06075 m.

Matching the scanning times, velocities and accelerations of the 2^{nd}-order and the 3^{rd}-order profiles with $a^{max}_{scan} = a$ and $s_{scan} = 1$, it is easy to show that

$$\tilde{T}_2 = T_1 + T_2 = 0.025$$
$$P_{scan} = 0.50\,T_1 + 0.25\,T_2 + 0.0545 \tag{16}$$

Authorized licensed use limited to: Eindhoven University of Technology. Downloaded on June 26,2023 at 08:45:42 UTC from IEEE Xplore. Restrictions apply.

Profile	Operation Time (OP) per Die	Thermal Loading		x_{off}	y_{off}	T_s	T_E
		Duration	Period				
Square	$\frac{2(2T_1+T_2)}{s_{scan}}+D+T_w+\frac{2(2T_1+T_2)}{s_{step}}+d+T_3$	D	$\frac{2(2T_1+T_2)}{s_{scan}}+T_w+T_3+\frac{2(2T_1+T_2)}{s_{step}}+d$	$\frac{2(2T_1+T_2)}{s_{scan}}+D+T_w+T_3$	$T_w+d+T_3+\frac{2(2T_1+T_2)}{s_{step}}$	$\frac{P_{T_s}}{V_{scan}}$	$D-\frac{P_{T_s}}{V_{scan}}$
Meander	$\frac{2(2T_1+T_2)}{s_{scan}}+D+T_3$	D	$\frac{2(2T_1+T_2)}{s_{scan}}+T_3$	$D+T_3$	T_3	$\frac{P_{T_s}}{V_{scan}}$	$D-\frac{P_{T_s}}{V_{scan}}$
Fillet	$\frac{2(2T_1+T_2)}{s_{scan}}+D+T_w$	D	$\frac{2(2T_1+T_2)}{s_{scan}}+T_w$	D	T_w	$\frac{P_{T_s}}{V_{scan}}$	$D-\frac{P_{T_s}}{V_{scan}}$

Fig. 8. A summary of *some* important operation quantities that can be used in optimization settings.

Assuming that $T_2 = k\,T_1$ with $k > 0 \in \mathbb{R}$, yields

$$\begin{aligned} T_1 &= \frac{0.025}{(k+1)} \\ P_{scan} &= 0.25\left(0.025\,\frac{(k+2)}{(k+1)}+0.218\right) \\ J_{scan} &= \frac{10(k+1)}{0.025} \leq 1600 \end{aligned} \tag{17}$$

Recalling Remark 2, the best value of k such that the difference $|P_{scan} - \tilde{P}_{scan}|$, i.e., between P_{scan} under 2^{nd} and 3^{rd}-order profiles, is the smallest possible under the constraint $J_{scan} \leq 1600\,\mathrm{m/s^3}$ is $k = 3$. Therefore, $T_1 = 0.00625\,\mathrm{s}$, and the profile total time is $0.218 + 2\,(2\,T_1 + T_2) = 0.2805\,\mathrm{s}$. This result confirms the possibility of maintaining finite jerk values when higher-order profiles are used [2], [6]. Also, it shows an overlooked cost associated with the needed operation time, which is equal to $0.268\,\mathrm{s}$ under the 2^{nd}-order profile [2], and it becomes $0.2805\,\mathrm{s}$ under the 3^{rd}-order profile, i.e., 1.047 times larger. Therefore, a trade-off between performance- affected by the maximum acceleration and jerk values- and throughput- affected by the operation time- is inevitable. This motivates us to formulate this relation in an optimization setting.

C. Physical Manifestation of Motion Profiles

In lithography machines, a motion profile is very vital. For example, in the mechanical domain, it appears as structural vibration or as errors in tracking and synchronization according to its frequency contents, see (2). Also, as a thermal loading in the thermal domain at the reticle [23], the wafer [13], [24], [25], the optics [26] through the light source illumination and the scanning time D, and at the motion actuators through repetitive motion. Moreover, a motion profile has a great influence on the machine *operation time* (OP) given in in Fig. 8, and the die yield, scheduling [27] and therefore the profit. To *partially* reduce the thermal loading at the affected parts, bounds on the scanning period and time D can be provided- see (11) and (12). This ensures the performance of existing active heat controlling systems [28]. To reduce the thermal load effect, its time, i.e., D, is minimized, and its period is maximized. Reducing the acceleration values at the actuators level reduces the thermal loading, especially if enough cooling time is provided. A summary of some vital operation quantities that can be optimized is given in Fig. 8. Any other quantity of interest must be written in terms of the reference motion parameters, see (4) to (11). The time-based *productivity ratio* of a profile (PR_P) is given as

$$PR_P = \frac{T_E}{OP} \times 100\% \tag{18}$$

which indicates the ratio of the productive time- during which profit is being made- to the overall operation time of a particular motion profile.

D. Optimizing the Step-and-Scan Profiles

When the motion profiles are optimized under a multidisciplinary design optimization setting, then the optimization problem gets harder to solve. This difficulty opens the way in front of machine and deep learning [29] to be used in designing trajectories. In this study, and due to the complexity associated with such a setting, we focus on optimizing the profiles' operation times such that the machine throughput can be increased while kinematical and temporal constraints are imposed. Using $T_1 = 0.00625, T_2 = 0.01875, T_3 = 0, k = 3$ to approximate the 2^{nd}-order profile in [2], $L = 0.032$, $W = 0.026$, $H = 0.01$ [2], and choosing $\epsilon_v = 0.0002$, $T_s \in [0.003, 0.007]\,\mathrm{s}$, $T_E \in [0.047, 0.193]\,\mathrm{s}$, and $n = m = 4$, then the optimization problem is given as

$$\begin{aligned} \min_{\theta\in\Theta}\ & \chi_1\,\mathcal{J}_1 + \sum_{i=2}^{c}\chi_i\,\mathcal{J}_i \\ s.t.\ & P_{scan}(\theta) = 0.0623125 \\ & P_{step}(\theta) = W + \epsilon_v \\ & -P(\theta) \leq -(L+H) \\ & 0 \leq a_{scan}^{max} \leq 200 \\ & 0 \leq a_{step}^{max} \leq 200 \\ & T_s^{min} \leq T_s \leq T_s^{max} \\ & T_E^{min} \leq T_E \leq T_E^{max} \\ & 0 \leq d \leq T_s^{max} + T_E^{max} \\ & 0 \leq T_w \leq T_s^{max} + T_E^{max} \\ & 0 < s_{scan} \leq 20 \\ & 0 < s_{step} \leq 20 \end{aligned} \tag{19}$$

Authorized licensed use limited to: Eindhoven University of Technology. Downloaded on June 26,2023 at 08:45:42 UTC from IEEE Xplore. Restrictions apply.

with $\mathcal{J}_1 = \left(OP(\theta) - \overline{OP}_i\right)^2$ denotes the objective index associated with *mainly* the operation time, and χ_1 is its associated weight, $\mathcal{J}_i, \forall i = 2, 3, \cdots, c$ denotes the objective indices associated with, e.g., the active thermal control systems, tracking errors, or light source written in terms of Θ, and χ_i are their corresponding weights. In this study, we focus on optimizing the operation time, and therefore we set $\chi_i = 0, \forall i = 2, 3, \cdots, c$. $\Theta = \{s_{scan}, s_{step}, a^{max}_{scan}, a^{max}_{step}, D, d, T_w\}$ is the set of decision variables, $\overline{OP}_i \in [0.1, 0.28]$ s is the desired operation time window and 0.001 is the minimum increment of $\overline{OP}_i$. Recalling Fig. 8, and (19), a nonlinear gradient-based solver can be used since both the objective function and constraints are continuous and have continuous first derivatives. In this study, the built-in MATLAB `fmincon` function is used. Consequently, a set of operating charts emerge and are used to select the machine operating points, as will be explained shortly.

Remark 4: Note that the concatenation of step and scan moves is affected by the actuators configuration used. When an actuator contributes to both the x and the y motions, the maximum current (power limit) that a single actuator draws can also be used in the objective function given in (19). This requires the actuators thermo-electro-mechanical model to be available. In this study, and *during only the optimization*, we do not impose any assumptions about the actuators coupling in the x-y motion.

III. Trajectory Generation and Dynamical Response

Recalling (2), it is possible to include a desired dynamical response of the controlled plant through the implementation of input shaping techniques [30], by simply having $\mathcal{F}(p(t)) = 0$ at the fundamental frequency. This is true if at least one of the needed conditions is satisfied, namely

$$\begin{aligned}
\sin\left(\pi\ f\ \frac{T_1}{s}\right) &= \sin\left(\pi\ \frac{\omega}{\omega_d}\right) \\
&= 0 \rightarrow \omega_d = \frac{2\,\pi\,s}{T_1} \\
\sin\left(\pi\ f\frac{T_1+T_2}{s}\right) &= \sin\left(\pi\,\frac{\omega}{\omega^*_d}\right) \\
&= 0 \rightarrow \omega^*_d = \frac{2\pi\,s}{T_1+T_2} \\
\sin\left(\pi\ f\ \left(\frac{2\,T_1+T_2}{s}+D\right)\right) &= \sin\left(\pi\ \frac{\omega}{\bar{\omega}^*_d}\right) = 0 \\
&\rightarrow \bar{\omega}^*_d = \frac{2\,\pi\,s}{2\,T_1+T_2+D\,s}
\end{aligned} \tag{20}$$

where $\omega_d, \omega^*_d, \bar{\omega}^*_d$ are the cutoff frequencies all in rad/s. Therefore, the closed-loop lightly damped natural frequency of the reticle and wafer stages can match the desired frequency obtained by the operating point using *pole placement*. Note that doing the same under (3) is more challenging. Recalling *Remark* 1, we have

$$\omega^{step}_d = \frac{2\,\pi\,s_{step}}{T_1}, \quad \omega^{scan}_d = \frac{2\,\pi\,s_{scan}}{T_1} \tag{21}$$

If the pole placement is not exact, then the resulting scaling factors can be calculated as

$$\tilde{s}_{step} = \frac{T_1\,\tilde{\omega}^{step}_d}{2\,\pi}, \quad \tilde{s}_{scan} = \frac{T_1\,\tilde{\omega}^{scan}_d}{2\,\pi} \tag{22}$$

and the new operating time can be found where $\tilde{\omega}^{step}_d$ and $\tilde{\omega}^{scan}_d$ are the obtained closed-loop lightly damped natural frequencies. This is how trajectory generation under input shaping affects other parameters or variables like V, D and OP. With $T_2 = 3\,T_1$, the OP of the proposed trajectories are given as

$$\begin{aligned}
\text{Square}: OP &= \frac{20\,\pi}{\omega^{scan}_d} + \frac{20\,\pi}{\omega^{step}_d} + D + T_w + d + T_3 \\
\text{Meander}: OP &= \frac{20\,\pi}{\omega^{scan}_d} + D + T_3 \\
\text{Fillet}: OP &= \frac{20\,\pi}{\omega^{scan}_d} + D + T_w
\end{aligned} \tag{23}$$

Similarly, the jerk values associated with the step-and-scan trajectories can be given as

$$J_{step} = \frac{a^{max}_{step}\,\omega^{step}_d}{2\,\pi}, \quad J_{scan} = \frac{a^{max}_{scan}\,\omega^{scan}_d}{2\,\pi} \tag{24}$$

Using $T_2 = k\,T_1$ with $k > 0 \in \mathbb{R}$ and ω^*_d in (20), yields

$$\omega_d = (1+k)\,\omega^*_d = \frac{2\,\pi\,(2+k)}{2\,\pi - D\,\bar{\omega}^*_d}\bar{\omega}^*_d \tag{25}$$

with $0 < \bar{\omega}^*_d < \frac{2\pi}{D}$, and V_{scan} is given as

$$\begin{aligned}
V_{scan} &= \frac{2^{max}_{scan}}{\omega^{*scan}_d} = \frac{2\pi\,(1+k)}{\omega^{scan}_d} a^{max}_{scan} \\
&= \left(\frac{2\pi}{\omega^{scan}_d}\right)^2 (1+k) J_{scan}
\end{aligned} \tag{26}$$

Also, P_{scan} can be given as

$$\begin{aligned}
P_{scan} &= \frac{2\,\pi\,(1+k)}{\left(\omega^{scan}_d\right)^2}\left(2\,\pi\,(2+k) + \omega^{scan}_d\,D\right) a^{max}_{scan} \\
&= \frac{4\,\pi^2(1+k)}{\left(\omega^{scan}_d\right)^3}\left(2\,\pi\,(2+k) + \omega^{scan}_d\,D\right) J_{scan}
\end{aligned} \tag{27}$$

Remark 5: Interestingly, (20) through (27) can be used to reformulate the previous kinematics-based optimization problem (19) such that plant dynamics and controllers parameters are involved. This will result in a kinodynamic-based optimization problem and *friendlier* trajectories to be followed.

1) Extrapolation of Trajectories: Recalling (6) and (21) with $T_2 = 3T_1$, the wafer stage point-to-point traverse, i.e. only stepping, motion to point $A_i\left(P_{x_i}, P_{y_i}\right)$ can be given as

$$\begin{aligned}
P_{x_i} &= \frac{8\,\pi\,\left(10\,\pi + d_{x_i}\,\tilde{\omega}^{step}_d\right)}{\left(\tilde{\omega}^{step}_d\right)^2}\,a^{max}_{x_i}\ \ meter \\
P_{y_i} &= \frac{8\,\pi\,\left(10\,\pi + d_{y_i}\,\tilde{\omega}^{scan}_d\right)}{\left(\tilde{\omega}^{scan}_d\right)^2}\,a^{max}_{y_i}\ \ meter
\end{aligned} \tag{28}$$

where under exact pole placement we have $\tilde{\omega}_d \equiv \omega_d$ for both step and scan variables. Therefore, for any P_{τ_i} and *suitable* constant velocity interval $d_{\tau_i} \geq 0$, the needed one dimensional

Authorized licensed use limited to: Eindhoven University of Technology. Downloaded on June 26,2023 at 08:45:42 UTC from IEEE Xplore. Restrictions apply.

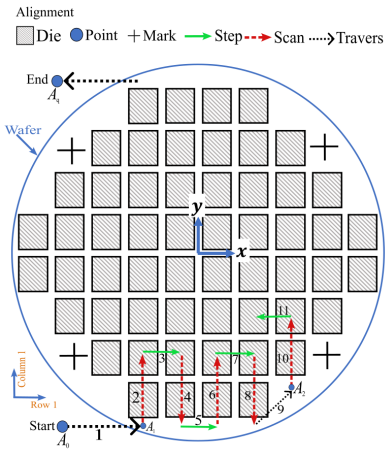

Fig. 9. A wafer substrate along with various traverse motions and step-and-scan trajectories.

traverse acceleration profiles- see segment 1 in Fig. 9- can be *generated* on-the-fly using (28) where $\tau \in \{x, y\}$, and the wafer stage traverse positioning profile in the τ-direction can be found by double integrating the corresponding acceleration profile. Note that d_{τ_i} is chosen such that $a_{\tau_i}^{max} \leq a_{\tau}^{max}$. The traverse timings associated with (28) under input shaping are given as

$$P_{x_i} \neq 0 : T_{x_i} = \frac{2\,(2\,T_1 + T_2)}{\tilde{s}_{step}} + d_{x_i} = \frac{20\,\pi}{\tilde{\omega}_d^{step}} + d_{x_i} \;\; second$$
$$P_{y_i} \neq 0 : T_{y_i} = \frac{2\,(2\,T_1 + T_2)}{\tilde{s}_{scan}} + d_{y_i} = \frac{20\,\pi}{\tilde{\omega}_d^{scan}} + d_{y_i} \;\; second \tag{29}$$

where $T_{\tau_i} = 0$ when $P_{\tau_i} = 0$. To realize two-dimensional traverse acceleration profiles, see segment 9 in Fig. 9, then $T_{x_i} = T_{y_i}$ must hold, i.e., time synchronization [31]. If the chosen d_{τ_i} ends up violating the bounds of $a_{\tau_i}^{max}$ calculated using (28), then the traverse point A_i must be recalculated. This is the essence of the *kinodynamic path planning* that will be covered separately in future work. The *total processing time* (T_P) of a wafer substrate is given as

$$T_P = N \times OP + \sum_{i=0}^{q} \max\{T_{x_i}, T_{y_i}\} + T_{i,idle} \tag{30}$$

where N and q are the numbers of dies in the substrate and the traverse points, respectively, and $T_{i,idle} \geq 0$ is the idle time after the i^{th} traverse motion. The machine throughput at the wafer substrate level is simply the reciprocal of (30). Excluding the preparation time T_s, the *productivity ratio* of the machine (PR_M) is given as

$$PR_M = \frac{N\,(D - T_s)}{T_L + T_A + T_P + T_U} \times 100\% \tag{31}$$

where T_L, T_A and T_U are the wafer substrate loading, alignment and unloading time intervals, respectively. A generic block diagram model of a reliable lithography machine is depicted in Fig. 10. This model can be used when studying related production lines, where the finite buffer size and the numerator of (31) can be used to give better estimates of the machine throughput [32].

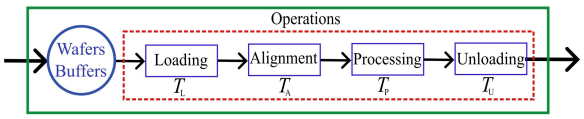

Fig. 10. Block diagram model of a *reliable* lithography machine.

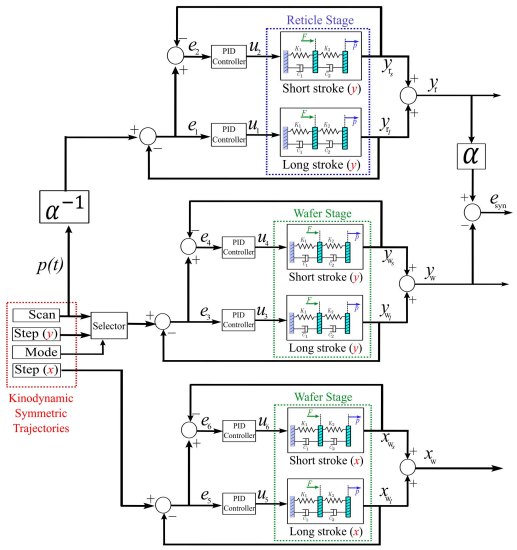

Fig. 11. The block diagram of a simplified wafer scanner machine using non-collocated cascaded motion stages.

2) Tracking and Closed-Loop Pole Placement: A typical lithography machine usually consists of cascaded non-collocated motion stages grouped in what can be referred to as open-chains [33]. Both the reticle and wafer chains consist of long and short strokes cascaded motion stages, while the optics chain comprises mainly passive elements with the possibility of having actively controlled mirrors. The reticle chain mainly covers the scanning motion in the y-direction, while the wafer chain moves in the x-y plane to cover stepping and scanning motions. During scanning phase, the reticle moves α^{-1} times faster than the wafer chain with typically $\alpha = 0.25$ as a lens magnification factor. More details can be found in [33]. The motion of the wafer scanner is approximated as shown in Fig. 11 with *decoupled axes of motion*, and we neglect the interaction with the optics chain. A detailed full chains interaction can be found in [33], [34]. In an attempt to enhance the performance of the wafer scanner machine, the following objective function can be mainly used within step-and-scan trajectories design phases- like (19):

$$\begin{aligned}\mathcal{J} = \sum_{i=1}^{6} \left\{ \gamma_i \, \max\left(e_i^2\right) + \beta_i \, \max\left(u_i^2\right) \right\} \\ + \gamma_7 \, \max\left(e_{syn}^2\right) + \gamma_8 \left(\omega_d^{scan} - \tilde{\omega}_d^{r_{ys}}\right)^2 \\ + \gamma_9 \left(\omega_d^{scan} - \tilde{\omega}_d^{w_{ys}}\right)^2 + \gamma_{10} \left(\omega_d^{step} - \tilde{\omega}_d^{w_{xs}}\right)^2 \\ + \gamma_{11} \left(\frac{\omega_d^{scan}}{(1+k)} - \tilde{\omega}_d^{r_{yl}}\right)^2 + \gamma_{12} \left(\frac{\omega_d^{scan}}{(1+k)} - \tilde{\omega}_d^{w_{yl}}\right)^2 \\ + \gamma_{13} \left(\frac{\omega_d^{step}}{(1+k)} - \tilde{\omega}_d^{w_{xl}}\right)^2 \end{aligned} \tag{32}$$

Authorized licensed use limited to: Eindhoven University of Technology. Downloaded on June 26,2023 at 08:45:42 UTC from IEEE Xplore. Restrictions apply.

where $\gamma_i, \beta_j \geq 0 \in \mathbb{R}$, $\tilde{\omega}_d^{r_{\tau_l}}, \tilde{\omega}_d^{r_{\tau_s}}, \tilde{\omega}_d^{w_{\tau_l}}, \tilde{\omega}_d^{w_{\tau_s}}$, are the reticle|wafer long ($r_{\tau_l}|w_{\tau_l}$) and short ($r_{\tau_s}|w_{\tau_s}$) lightly damped frequencies in the τ-direction, and other variables are clear from Fig. 11. Here, ω_d is associated with the reticle and wafer short strokes while ω_d^* is associated with their long strokes. Note that x_w and the traverse motion associated errors are crucial once the complete trajectories at the wafer substrate level are considered, and therefore can be added to (32). In (32), we *initially* assign ω_d to the short strokes and ω_d^* to the long strokes, while $\bar{\omega}_d^*$ can be used with the machine base frame anti-vibration system when it is included in the machine model.

3) The Orders of Motion Profiles: In (1), a 3^{rd}-order motion profile was used based on which this study was formulated. Having the motion profile power spectrum in (2) followed by the requirements of input shaping technique given in (20), we ended up having ω_d^{step} and ω_d^{scan} and their associated $\omega_d^*, \bar{\omega}_d^*$ frequencies. Under the fillet motion profile, both ω_d^{step} and ω_d^{scan} are identical, which resulted in having the three short strokes shown in Fig. 11 to operate at the same frequency under input shaping and closed-loop control. However, under the meander and possibly the square profiles, ω_d^{step} and ω_d^{scan} can be distinct, and therefore the wafer stage closed-loop system can be asymmetric along the x and y directions. Obviously, when other control techniques are used like feed-forward [35], asymmetric stages design is involved, more lightly damped modes or alignment process are considered, or the dynamics of the wafer substrates and reticle masks handling systems are included, see Fig. 10, then the used motion profiles should have more frequency contents to be exploited. Hence, this motivates higher-order profiles investigation in future work.

4) The Complete Trajectories: Fig. 9 shows a wafer substrate that consists of replicas of dies whose number is maximized based on the desired die dimensions, the vertical ϵ_v and horizontal ϵ_h scribe lanes dimensions, substrate radius and other factors as well [36], [37]. To realize the exposure process of these dies, a concatenation of traverse and step-and-scan motions can be designed using path planning, which results in traverse points $A_i, i = 1, 2, \cdots, q$ shown in Fig. 9. Using the analytical expression given in (28), the traverse motions, eg. 1 and 9, can be obtained, while the step-and-scan motions, eg. segments 2 through 8, 10 and 11, can be obtained using the previously developed motion profiles.

5) Machine Performance: Two important specifications for lithography machines are the contrast and overlay measures. Overlay is defined as the ability of the lithography machine to expose two images on top of each other [2]. Overlay correlates with the lower-frequency part of the positioning errors of the stages during exposure, and it can be represented using moving average MA [2] filtering. Contrast can be partly characterized by moving standard deviation MSD filtering, resulting in the higher-frequency part of the positioning errors during exposure [2].

For 38-nm half-pitch lithography typically, the MA $\leq$ 1 nm, and the MSD $\leq$ 7 nm [2]. Since the reticle stage moves α^{-1} times faster than the wafer stage, using the same profile $p(t)$ during scanning, both MA and MSD can be used to define the synchronization error during a scanning period in the y-direction as

$$\mathrm{MA}_r = \frac{1}{T}\int_{-\frac{T}{2}}^{\frac{T}{2}} \left(\alpha^{-1}\, p(t) - y_r\right) dt \tag{33}$$

$$\mathrm{MA}_w = \frac{1}{T}\int_{-\frac{T}{2}}^{\frac{T}{2}} \left(p(t) - y_w\right) dt \tag{34}$$

where T *usually* represents the actual exposure time, i.e. $D - T_s$; however, we used $T \equiv OP$ to evaluate the performance indices. The synchronization error is given as

$$e_{\mathrm{syn}} = \alpha\, y_r - y_w \tag{35}$$

and its associated MA is given as

$$\mathrm{MA}_{\mathrm{syn}} = \mathrm{MA}_w - \alpha\, \mathrm{MA}_r \tag{36}$$

Similarly, the synchronization error MSD is given as

$$\mathrm{MSD}_{\mathrm{syn}} = \sqrt{\frac{1}{T}\int_{-\frac{T}{2}}^{\frac{T}{2}} \left(e_{\mathrm{syn}}(t) - \mathrm{MA}_{\mathrm{syn}}\right)^2 dt} \tag{37}$$

IV. Simulation

Using Fig. 8 and by solving (19) $\forall \overline{OP}_i$, the optimal solutions were obtained and used to generate the operating charts given by Fig. 12 and Fig. 13. Then, the responses of the simplified wafer scanner machine shown in Fig. 11 under *only* the meander and fillet step-and-scan motion profiles are obtained, where the needed PID controllers parameters are obtained through minimizing the objective function given in (32) using *particle swarm optimization* with $\gamma_i = 10, \beta_i = 0, i = 1, 2, \cdots, 6$, $\gamma_7 = 10$ and $\gamma_l = 10^5, l = 8, \cdots, 13$. The stages and controllers parameters are given in appendices B and C, respectively. The operating points selected in Fig. 12 are used in (21) to obtain the desired frequencies. Despite being useful, the machine response due to the square profile is excluded in this specific example; because it violates one design requirement within the desired OP window.

A. Selection of Operating Point

The set of optimal solutions can be used to select the best machine operating conditions. It also helps in appreciating the level of complexity associated with the reference motion design process. From Fig. 12 and by using $J_{scan} \leq 1600\,\mathrm{m/s^3}$ as the selection criterion of the machine operating point, it is clear that the square profile fails to meet the jerk limits needed, and therefore got excluded (the least value is $1870 > 1600\,\mathrm{m/s^3}$). The nearest operating point under the meander profile is at $OP = 0.195\,\mathrm{s}$, and under the fillet profiles is at $OP = 0.23\,\mathrm{s}$, which are less than the original $OP = 0.268\,\mathrm{s}$ of the 2^{nd}-order profile in [2], and the 3^{rd}-order profile before optimization, i.e. $OP = 0.2805\,\mathrm{s}$. From Fig. 12 and Fig. 13, it is clear that the $OP, a_{scan}^{max}, V, x_{off}$ operating conditions under the meander profile are better than those under the fillet profile, while the opposite is true with $y_{off} = T_3 = 0$ and the thermal duration and period. When $y_{off} = T_3 = 0.035\,\mathrm{s}$, then the meander and the fillet profiles have the

Authorized licensed use limited to: Eindhoven University of Technology. Downloaded on June 26,2023 at 08:45:42 UTC from IEEE Xplore. Restrictions apply.

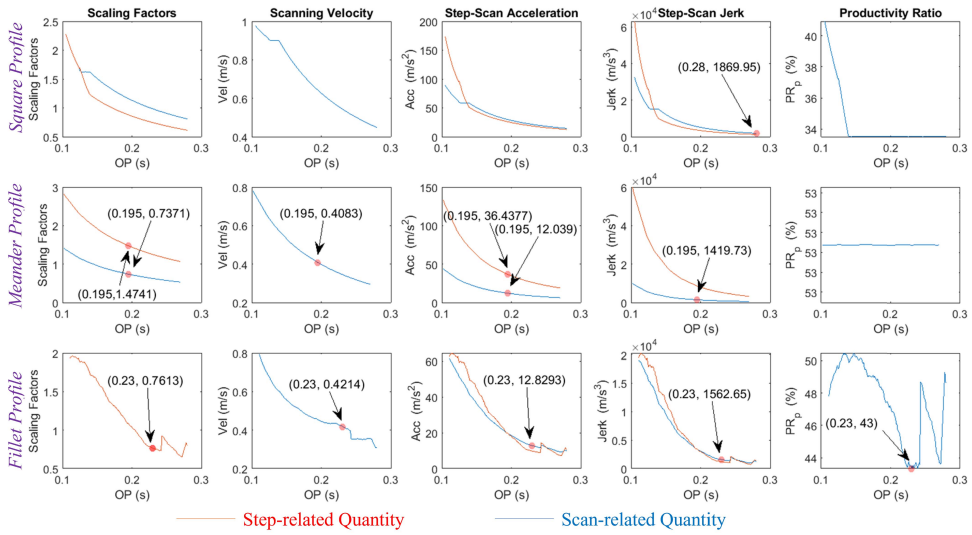

Fig. 12. The selection of an operating point from the set of optimal solutions of the proposed 3^{rd}-order profiles when $T_3 = 0$. It also shows the scaling factors, scanning velocity, accelerations, jerk values, and the profiles productivity ratios.

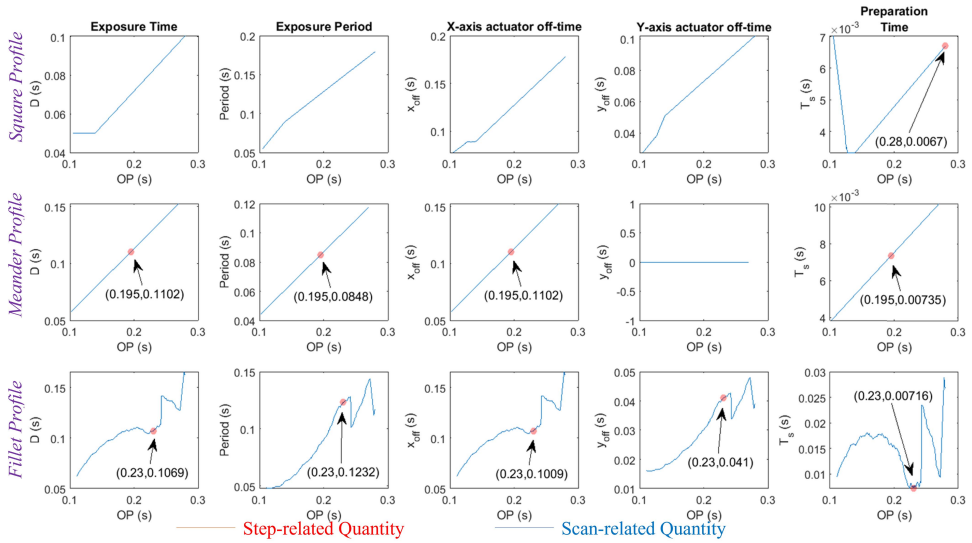

Fig. 13. The selection of an operating point from the set of optimal solutions of the proposed 3^{rd}-order profiles when $T_3 = 0$. It also shows the exposure duration and period, the x, y actuators off-time values, and the preparation time.

same OP. Using (11), We find that for the meander profile $T_s \approx 7.3 \times 10^{-3}$ s and for the fillet profile $T_s \approx 7.1 \times 10^{-3}$ s. Moreover, PR_P of the meander profile is 52.77% while for the fillet profile is 43.39%. Fig. 14 shows the trajectories of the proposed profiles in the x-y plane at the first common $OP = 0.134$ s [20], and second common $OP = 0.232$ s whose associated numeric values are given in TABLE I. Note that using TABLE I and $d \equiv T_w \approx 0.0413$ s with the fillet profile and zero otherwise, various quantities can be calculated, if desired. Also, several operating conditions can be stored in lookup tables for validation or future use. Selecting the machine operating point based on other selection criteria follows in a similar fashion where additional constraints can be imposed, and jointly addressed.

TABLE I

NUMERIC RESULTS ASSOCIATED WITH THE MOTION PROFILES WHEN OPERATED AT 0.232 s, ROUNDED TO TWO DIGITS

Profile	a_{scan}^{max}	a_{step}^{max}	s_{scan}	s_{step}	D
Square	21.07	18.30	0.98	0.74	0.083
Meander	8.51	25.74	0.62	1.24	0.131
Fillet	12.62	9.58	0.76	0.76	0.108

The machine performance under the 2^{nd}-order trajectory- whose jerk values are infinite- is depicted in Fig. 15. Comparing this to the case of finite jerk values realized using

Authorized licensed use limited to: Eindhoven University of Technology. Downloaded on June 26,2023 at 08:45:42 UTC from IEEE Xplore. Restrictions apply.

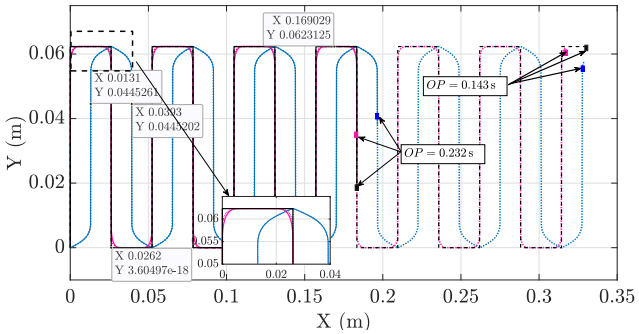

Fig. 14. The step-and-scan trajectories of the square (black), the meander (blue), and the fillet (magenta) profiles in the x-y plane when $OP = 0.134$ s [20] (dotted lines), and $OP = 0.232$ s (solid lines). The colored squares mark the ends of their corresponding profiles. Notice how OP affects the roundness in the fillet profile, and *generally* the throughput when all profiles under the two operating points are simulated for 1.72 s.

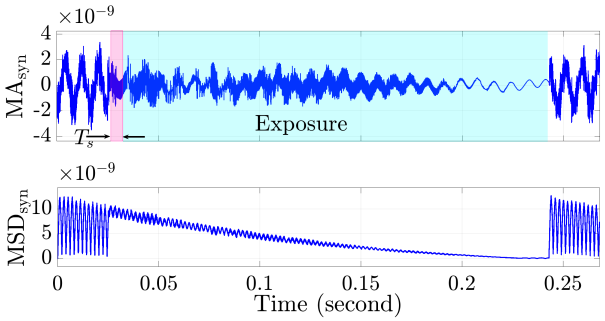

Fig. 15. Performance indices under the 2^{nd}-order profiles of a single die. The controllers parameters obtained for the 3^{rd}-order fillet step-and-scan profile were used.

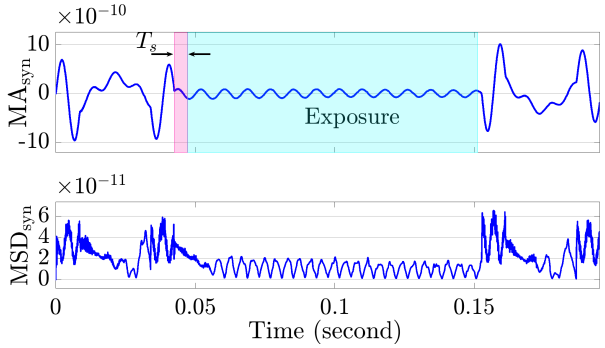

Fig. 16. Performance indices under the 3^{rd}-order meander step-and-scan profiles of a single die.

3^{rd}-order trajectories, Fig. 16 shows the machine performance under the meander profile, while Fig. 17 shows its performance under the fillet profile. Clearly, the latter performance is better than the 2^{nd}-order and the meander profiles. In the fillet profile, exact pole placement was achieved only for the short strokes. From these figures, the advantage of increasing the reference trajectory order on the synchronization error is obvious. In fact, this advantage is possible only if the optics system can handle a reduction of D from 0.218 s under the 2^{nd}-order profile to 0.1069 s with $T_s \approx 0.017$ s under the fillet profile, such that the light source is ready to the next exposure cycle. This point should reflect the complexity of the investigated optimization problem.

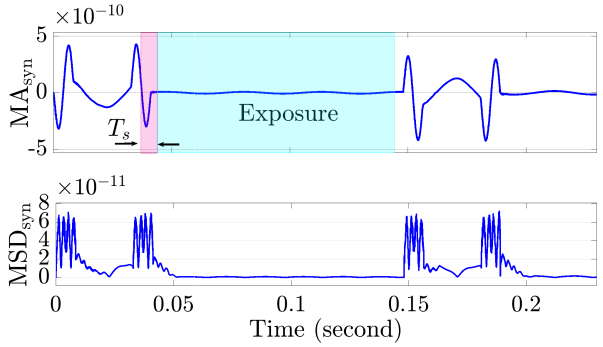

Fig. 17. Performance indices under the 3^{rd}-order fillet step-and-scan profiles of a single die.

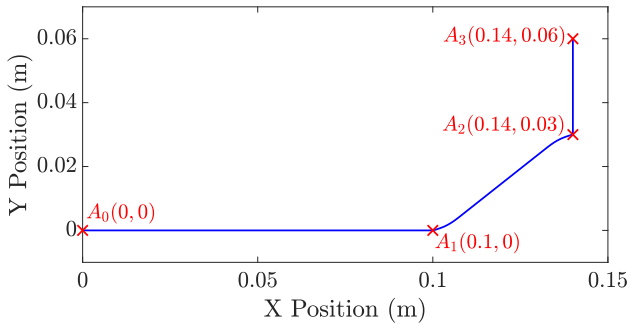

Fig. 18. Various wafer stage traverse motions in the x-y plane.

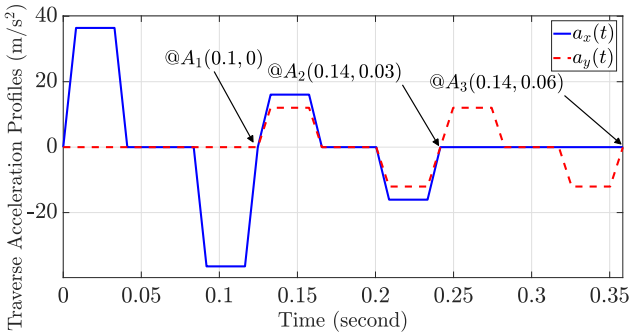

Fig. 19. The wafer stage traverse acceleration profiles needed to generate the motion depicted in Fig. 18.

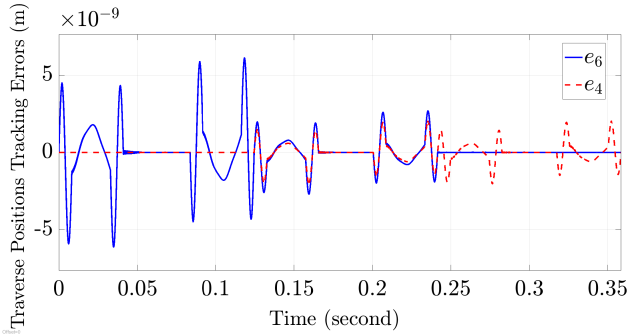

Fig. 20. The wafer stage traverse motion tracking errors under the motion depicted in Fig. 18.

Fig. 18 shows various wafer stage traverse motions in the x-y plane where the controllers parameters obtained for the fillet profile are used. Using (28) and (29), the needed

Authorized licensed use limited to: Eindhoven University of Technology. Downloaded on June 26,2023 at 08:45:42 UTC from IEEE Xplore. Restrictions apply.

acceleration profiles were generated easily with $a_x^{max} = 36.4377\,\mathrm{m/s^2}$ and $a_y^{max} = 12.0387\,\mathrm{m/s^2}$ selected in Fig. 12 under the meander profile; to reduce the transition time between dies. The traverse steps acceleration in the x and y directions, i.e., $a_x(t), a_y(t)$, are depicted in Fig. 19, and the wafer stage traverse motion tracking error is shown in Fig. 20. From these figures, the strength of the proposed framework in extrapolating the trajectory generation process on-line is made evident.

V. Conclusion and Future Work

In this investigation, we proposed a framework to design the reference motion profiles used in wafer scanners. Specifically, the step-and-scan profiles are the heartbeats of a lithography machine with which all- not only motion-related-subsystems have to be synchronized. Therefore, we proposed an optimization framework where all the subsystems requirements and limitations can be jointly addressed in a multi-disciplinary design optimization setting. After formulating kinematics-based optimization problems, the optimal machine operating points were obtained under different motion profiles. Then, the closed-loop controllers were optimized such that the lightly damped modes of the driven stages matches the ones associated with the selected operating points under the input shaping technique. In light of the proposed trajectory generation framework, we advocated the use of higher-order motion profiles while taking into consideration the effect on the operation time and machine throughput.

Currently, we are looking into kinodynamical path planning to process a wafer substrate in the wafer scanner while considering the relation between the profile order, the operating conditions, and the machine dynamics when a large number of uncertain lightly-damped modes are involved.

Appendix A
Symbolic Values

Note: Use $\bar{a} \in \{a, a_{step}^{max}, a_{scan}^{max}\}, \bar{s} \in \{s, s_{step}, s_{scan}\}$, and $\bar{D} \in \{D, d\}$, based on the used motion type, i.e., step or scan.

$$\alpha_3^1 = \alpha_3^7 = \frac{\bar{a}\,\bar{s}}{6\,T_1},\ \alpha_3^2 = \alpha_3^4 = \alpha_3^6 = 0$$
$$\alpha_3^3 = \alpha_3^5 = -\alpha_3^1,\ \alpha_2^1 = \alpha_2^4 = 0\ \alpha_2^2 = \frac{a}{2}$$
$$\alpha_2^3 = \frac{\bar{a}\,(2\,T_1 + T_2)}{2\,T_1}$$
$$\alpha_2^5 = \frac{\bar{a}\,\left(2\,T_1 + T_2 + \bar{D}\,\bar{s}\right)}{2\,T_1}$$
$$\alpha_2^6 = -\alpha_2^2$$
$$\alpha_2^7 = -\alpha_2^3$$
$$\alpha_1^1 = 0$$
$$\alpha_1^2 = -\frac{T_1\,a}{2\,\bar{s}}$$
$$\alpha_1^3 = -\frac{\bar{a}\,\left(2\,{T_1}^2 + 2\,T_1\,T_2 + {T_2}^2\right)}{2\,T_1\,\bar{s}}$$
$$\alpha_1^4 = \frac{\bar{a}\,(T_1 + T_2)}{\bar{s}}$$
$$\alpha_1^5 = -\frac{\bar{a}\,\bar{s}}{2\,T_1}\,\bar{D}^2 - \frac{\bar{a}\,(2\,T_1 + T_2)}{T_1}\,\bar{D} - \frac{\bar{a}\,\left(2\,{T_1}^2 + 2\,T_1\,T_2 + {T_2}^2\right)}{T_1\,\bar{s}\,2}$$
$$\alpha_1^6 = \frac{\bar{a}\,\left(7\,T_1 + 4\,T_2 + 2\,\bar{D}\,\bar{s}\right)}{2\,\bar{s}}$$
$$\alpha_1^7 = \frac{\bar{a}\,\left(4\,T_1 + 2\,T_2 + \bar{D}\,\bar{s}\right)^2}{2\,T_1\,\bar{s}}$$
$$\alpha_0^1 = 0$$
$$\alpha_0^2 = \frac{{T_1}^2\,a}{6\,\bar{s}^2}$$
$$\alpha_0^3 = \frac{\bar{a}\,\left(2\,{T_1}^3 + 3\,{T_1}^2\,T_2 + 3\,T_1\,{T_2}^2 + {T_2}^3\right)}{6\,T_1\,\bar{s}^2}$$
$$\alpha_0^4 = -\frac{\bar{a}\,\left(2\,{T_1}^2 + 3\,T_1\,T_2 + {T_2}^2\right)}{2\,\bar{s}^2}$$
$$\alpha_0^5 = \frac{\bar{a}\,\bar{s}}{6\,T_1}\,\bar{D}^3 + \frac{\bar{a}\,(2\,T_1 + T_2)}{2\,T_1}\,\bar{D}^2 + \frac{\bar{a}\,\left(4\,{T_1}^2 + 4\,T_1\,T_2 + {T_2}^2\right)}{2\,T_1\,\bar{s}}\,\bar{D} + \frac{\bar{a}\,\left(2\,{T_1}^3 + 3\,{T_1}^2\,T_2 + 3\,T_1\,{T_2}^2 + {T_2}^3\right)}{6\,T_1\,\bar{s}^2}$$
$$\alpha_0^6 = -\frac{a}{2}\,\bar{D}^2 - \frac{\bar{a}\,(15\,T_1 + 6\,T_2)}{6\,\bar{s}}\,\bar{D} - \frac{\bar{a}\,\left(25\,{T_1}^2 + 24\,T_1\,T_2 + 6\,{T_2}^2\right)}{6\,\bar{s}^2}$$
$$\alpha_0^7 = -\frac{\bar{a}\,\bar{s}}{6\,T_1}\,\bar{D}^3 - \frac{\bar{a}\,(2\,T_1 + T_2)}{T_1}\,\bar{D}^2 - \frac{\bar{a}\,\left(7\,{T_1}^2 + 7\,T_1\,T_2 + 2\,{T_2}^2\right)}{T_1\,\bar{s}}\,\bar{D} - \frac{\bar{a}\,\left(52\,{T_1}^3 + 78\,{T_1}^2\,T_2 + 42\,T_1\,{T_2}^2 + 8\,{T_2}^3\right)}{6\,T_1\,\bar{s}^2}$$

Appendix B
Stages Parameters

The reticle stage long stroke parameters are $m_1 = 42.5\,Kg, m_2 = 8\,Kg, k_1 = 10\,N/m, k_2 = 7\,N/m, c_1 = 10\,Ns/m, c_2 = 80\,Ns/m$, and the wafer stage long stroke parameters in x and y directions are $m_1 = 47.0\,Kg, m_2 = 15\,Kg, k_1 = 16\,N/m, k_2 = 10\,N/m, c_1 = 15\,Ns/m, c_2 = 105\,Ns/m$. The short strokes parameters of the two stages are halves of their corresponding long strokes parameters.

Appendix C
Controllers Parameters

The PID controller transfer function in the frequency domain is given as

$$G_{PID}(s) = K_P + \frac{K_I}{s} + \frac{K_D\,N_F}{s + N_F}\,s$$

where s denotes the complex frequency- *not a time scaling factor*-, K_P, K_I, K_D and N_F are the proportional, the integral, the derivative and the filter coefficients, respectively.

Authorized licensed use limited to: Eindhoven University of Technology. Downloaded on June 26,2023 at 08:45:42 UTC from IEEE Xplore. Restrictions apply.

TABLE II

RETICLE STAGE LONG STROKE (ROUNDED) CONTROLLER PARAMETERS UNDER MEANDER (M) AND FILLET (F) PROFILES

Profile	$K_P/10^9$	$K_I/10^{14}$	$K_D/10^{10}$	$N_F/10^{10}$
M	2.7	4.8	1.4	7.1
F	0.7	1.7	0.5	7.2

TABLE III

RETICLE STAGE SHORT STROKE (ROUNDED) CONTROLLER PARAMETERS UNDER MEANDER (M) AND FILLET (F) PROFILES

Profile	$K_P/10^8$	$K_I/10^{10}$	$K_D/10^6$	$N_F/10^7$
M	2.0	1.7	117	7902
F	0.1	0.1	1.2	3.7

TABLE IV

WAFER STAGE y-DIRECTION LONG STROKE (ROUNDED) CONTROLLER PARAMETERS UNDER MEANDER (M) AND FILLET (F) PROFILES

Profile	$K_P/10^8$	$K_I/10^{14}$	$K_D/10^9$	$N_F/10^9$
M	34	3.5	10	89
F	1.3	3.2	8.6	2.1

TABLE V

WAFER STAGE y-DIRECTION SHORT STROKE (ROUNDED) CONTROLLER PARAMETERS UNDER MEANDER (M) AND FILLET (F) PROFILES

Profile	$K_P/10^6$	$K_I/10^9$	$K_D/10^6$	$N_F/10^9$
M	3.1	5.7	1.8	7.6
F	9.4	1.4	2.0	0.9

TABLE VI

WAFER STAGE x-DIRECTION LONG STROKE (ROUNDED) CONTROLLER PARAMETERS UNDER MEANDER (M) AND FILLET (F) PROFILES

Profile	$K_P/10^8$	$K_I/10^{14}$	$K_D/10^9$	$N_F/10^9$
M	6.8	0.002	0.09	76.1
F	1.3	3.2	8.6	2.1

TABLE VII

WAFER STAGE x-DIRECTION SHORT STROKE (ROUNDED) CONTROLLER PARAMETERS UNDER MEANDER (M) AND FILLET (F) PROFILES

Profile	$K_P/10^6$	$K_I/10^9$	$K_D/10^6$	$N_F/10^9$
M	30.1	531	7.6	63.4
F	9.4	1.4	2.0	0.9

REFERENCES

[1] M. F. Heertjes, B. Van Der Velden, and T. Oomen, "Constrained iterative feedback tuning for robust control of a wafer stage system," *IEEE Trans. Control Syst. Technol.*, vol. 24, no. 1, pp. 56–66, Jan. 2016.

[2] H. Butler, "Position control in lithographic equipment," *IEEE Control Syst. Mag.*, vol. 31, no. 5, pp. 28–47, Oct. 2011.

[3] A. Haber, "Estimation and control of large-scale systems with an application to adaptive optics for EUV lithography," Ph.D. dissertation, Delft Center Syst. Control. TU Delft, Delft Univ. Technol., Delft, Netherlands, 2014.

[4] C. Mack, *Fundamental Principles of Optical Lithography: The Science of Microfabrication*. Hoboken, NJ, USA: Wiley, 2008.

[5] R.-H.-M. Schmidt, "Ultra-precision engineering in lithographic exposure equipment for the semiconductor industry," *Phil. Trans. Roy. Soc. A, Math., Phys. Eng. Sci.*, vol. 370, no. 1973, pp. 3950–3972, Aug. 2012.

[6] P. Lambrechts, M. Boerlage, and M. Steinbuch, "Trajectory planning and feedforward design for electromechanical motion systems," *Control Eng. Pract.*, vol. 13, no. 2, pp. 145–157, 2005.

[7] B. G. Dijkstra and O. H. Bosgra, "Exploiting iterative learning control for input shaping, with application to a wafer stage," in *Proc. Amer. Control Conf. (ACC)*, 2003, pp. 4811–4815.

[8] K. Bos, D. Heck, R. Van Der Kall, and M. Heertjes, "Input-output linearized control of a thermoelectric actuator using an extended Kalman filter observer," in *Proc. Euspen Special Interest Group Meeting, Thermal Issues*, Aachen, Germany, 2020, pp. 1–4.

[9] V. Ryaboy, *Vibration Control for Optomechanical Systems*. Chennai, Tamil Nadu: World Scientific Publishing Company Incorporated, 2021.

[10] J. Chang, C. J. Martin, R. L. Engelstad, and E. G. Lovell, "Thermomechanical global response of the EUVL wafer during exposure," *Proc. SPIE*, vol. 4688, pp. 755–766, Jul. 2002.

[11] J. Dai, J. Xia, C. Wang, and S. Xu, "Thermal analysis of an electromagnetic linear actuator," *Adv. Mech. Eng.*, vol. 9, no. 12, Dec. 2017, Art. no. 168781401774538.

[12] P. Chen, W. Wang, and S. Lin, "Thermal effect induced wafer deformation in high-energy e-beam lithography," in *Alternative Lithographic Technologies VII*, D. J. Resnick and C. Bencher, Eds., vol. 9423. Bellingham, WA, USA: SPIE, 2015, pp. 189–201.

[13] L. Subramany *et al.*, "Analysis of wafer heating in 14 nm DUV layers," in *Metrology, Inspection, and Process Control for Microlithography*, M. I. Sanchez, Ed., vol. 9778. Bellingham, WA, USA: SPIE, 2016, pp. 275–281.

[14] B. Sencer and S. Tajima, "Frequency optimal feed motion planning in computer numerical controlled machine tools for vibration avoidance," *J. Manuf. Sci. Eng.*, vol. 139, no. 1, Jan. 2017.

[15] M. F. Heertjes *et al.*, "Control of wafer scanners: Methods and developments," in *Proc. Amer. Control Conf. (ACC)*, Jul. 2020, pp. 3686–3703.

[16] D. Bruijnen and N. Van Dijk, "Combined input shaping and feedforward control for flexible motion systems," in *Proc. Amer. Control Conf. (ACC)*, Jun. 2012, pp. 2473–2478.

[17] F. Boeren, D. Bruijnen, N. Van Dijk, and T. Oomen, "Joint input shaping and feedforward for point-to-point motion: Automated tuning for an industrial nanopositioning system," *Mechatronics*, vol. 24, no. 6, pp. 572–581, Sep. 2014.

[18] N. C. Singer and W. P. Seering, "Preshaping command inputs to reduce system vibration," *ASME J. Dyn. Syst., Meas., Control*, vol. 112, no. 1, pp. 76–82, 1990.

[19] B. Sencer, K. Ishizaki, and E. Shamoto, "High speed cornering strategy with confined contour error and vibration suppression for CNC machine tools," *CIRP Ann.*, vol. 64, no. 1, pp. 369–372, 2015.

[20] Y. M. Al-Rawashdeh, M. Al Janaideh, and M. Heertjes, "On step-and-scan trajectories used in wafer scanners in semiconductor manufacturing," in *Proc. IEEE/RSJ Int. Conf. Intell. Robots Syst. (IROS)*, Sep. 2021, pp. 7580–7586.

[21] P. M. Swamidass, *Machine Reliability*. Boston, MA, USA: Springer, 2000, p. 384.

[22] K.-H. Rew and K.-S. Kim, "A closed-form solution to asymmetric motion profile allowing acceleration manipulation," *IEEE Trans. Ind. Electron.*, vol. 57, no. 7, pp. 2499–2506, Jul. 2010.

[23] C. Bikcora, S. Weiland, and W. M. J. Coene, "Thermal deformation prediction in reticles for extreme ultraviolet lithography based on a measurement-dependent low-order model," *IEEE Trans. Semicond. Manuf.*, vol. 27, no. 1, pp. 104–117, Feb. 2014.

[24] M. Cho, Y. Lee, S. Joo, and K. S. Lee, "Semi-empirical model-based multivariable iterative learning control of an RTP system," *IEEE Trans. Semicond. Manuf.*, vol. 18, no. 3, pp. 430–439, Aug. 2005.

[25] J. M. Muganda, B. Jansen, E. Homburg, Y. Van De Burgt, and J. Den Toonder, "Influence function measurement technique using the direct and indirect piezoelectric effect for surface shape control in adaptive systems," *IEEE Trans. Autom. Sci. Eng.*, vol. 19, no. 2, pp. 1–9, Feb. 2021.

Authorized licensed use limited to: Eindhoven University of Technology. Downloaded on June 26,2023 at 08:45:42 UTC from IEEE Xplore. Restrictions apply.

[26] B. Zhu *et al.*, "Fast thermal aberration model for lithographic projection lenses," *Opt. Exp.*, vol. 27, no. 23, pp. 34038–34049, Nov. 2019.
[27] B. Yan, H. Y. Chen, P. B. Luh, S. Wang, and J. Chang, "Litho machine scheduling with convex hull analyses," *IEEE Trans. Autom. Sci. Eng.*, vol. 10, no. 4, pp. 928–937, Oct. 2013.
[28] D. Van Den Hurk, S. Weiland, and K. Van Berkel, "Performance-based active wafer clamp design for wafer heating effects in EUV lithography," *IEEE Trans. Semicond. Manuf.*, vol. 33, no. 3, pp. 424–432, Aug. 2020.
[29] F. L. De La Rosa, R. Sánchez-Reolid, J. L. Gómez-Sirvent, R. Morales, and A. Fernández-Caballero, "A review on machine and deep learning for semiconductor defect classification in scanning electron microscope images," *Appl. Sci.*, vol. 11, no. 20, p. 9508, Oct. 2021.
[30] B. G. Dijkstra, N. J. Rambaratsingh, C. Scherer, O. H. Bosgra, M. Steinbuch, and S. Kerssemakers, "Input design for optimal discrete time point-to-point motion of an industrial XY-positioning table," in *Proc. 39th IEEE Conf. Decis. Control*, 2000, pp. 901–906.
[31] Y. Fang, J. Hu, W. Liu, Q. Shao, Q. Jin, and Y. Peng, "Smooth and time-optimal S-curve trajectory planning for automated robots and machines," *Mechanism Mach. Theory*, vol. 137, pp. 127–153, Jul. 2019.
[32] K. Park and J. R. Morrison, "Controlled wafer release in clustered photolithography tools: Flexible flow line job release scheduling and an LMOLP heuristic," *IEEE Trans. Autom. Sci. Eng.*, vol. 12, no. 2, pp. 642–655, Apr. 2015.
[33] Y. M. Al-Rawashdeh, M. Al-Tamimi, M. Heertjes, and M. A. Janaideh, "Micro-positioning end-stage for precise multi-axis motion control in optical lithography machines: Preliminary results," in *Proc. Amer. Control Conf. (ACC)*, May 2021, pp. 40–47.
[34] Y. M. Al-Rawashdeh, M. A. Janaideh, and M. Heertjes, "On synchronization of generic lithography machine open-chains using a novel fine-positioning stage system," in *Proc. IEEE Conf. Control Technol. Appl. (CCTA)*, Aug. 2021, pp. 1089–1094.
[35] H. Butler, "Adaptive feedforward for a wafer stage in a lithographic tool," *IEEE Trans. Control Syst. Technol.*, vol. 21, no. 3, pp. 875–881, May 2013.
[36] R. M. Best and S. K. Tiku, "Gross die per wafer and yield optimization for GaAs ICs with sub-micron features," *IEEE Trans. Semicond. Manuf.*, vol. 32, no. 4, pp. 518–522, Nov. 2019.
[37] J.-S. Kim, S.-J. Jang, T.-W. Kim, H.-J. Lee, and J.-B. Lee, "A productivity-oriented wafer map optimization using yield model based on machine learning," *IEEE Trans. Semicond. Manuf.*, vol. 32, no. 1, pp. 39–47, Feb. 2019.

Yazan M. Al-Rawashdeh received the B.Sc. degree in mechatronics engineering from The University of Jordan (UJ), Amman, Jordan, in 2006, and the M.Sc. and Ph.D. degrees in systems and control engineering from the King Fahd University of Petroleum and Minerals (KFUPM), Dhahran, Saudi Arabia, in 2014 and 2018, respectively. He is currently a Post-Doctoral Fellow with the Department of Mechanical and Mechatronics Engineering, Memorial University (MUN), St John's, NL, Canada. His current research interests are control of multi-agent systems and semiconductor manufacturing.

Mohammad Al Janaideh received the M.A.Sc. and Ph.D. degrees in mechanical engineering (mechatronics and control) from Concordia University, Canada. He was a Post-Doctoral Fellow with the Department of Electrical and Computer Engineering, University of Toronto, and the Department of Aerospace Engineering, University of Michigan, Ann Arbor. He was a Visiting Professor with the Institute of Mathematics, Czech Academy of Sciences, Prague, Université de Franche-Comté (UFC), Sorbonne Université, France, and the Center for Research on Complex Automated Systems, University of Bologna. He also worked as a Senior Mechatronics Engineer at ASML, CT, USA. Since 2017, he has been with the Department of Mechanical Engineering, Memorial University, St John's, NL, Canada, where he is currently an Associate Professor in mechatronics and control with the Department of Mechanical and Mechatronics Engineering. He is also with the Department of Electrical and Computer Engineering, University of Toronto. His research interests include the design and control of micro- and nano-positioning systems, fault detection and mitigation of connected autonomous robotics networks, design and control of precision motion stages for semiconductor manufacturing machines, and control of systems with uncertain hysteresis nonlinearities. He is a Technical Editor of IEEE TRANSACTIONS ON MECHATRONICS, IEEE Conference of Decision and Control (CDC), the American Control Conference (ACC), ASME Dynamic Systems and Control Conference (DSCC), and IFAC Modeling, Estimation, and Control Conference (MECC).

Marcel F. Heertjes received the M.Sc. and Ph.D. degrees in mechanical engineering from the Eindhoven University of Technology, Eindhoven, The Netherlands, in 1995 and 1999, respectively. In 2000, he joined the Philips Center for Industrial Technology, Eindhoven. In 2007, he joined ASML, Mechatronics Development, Veldhoven, The Netherlands, and the Control System Technology and the Dynamics and Control groups, Department of Mechanical Engineering, Eindhoven University of Technology, where he was a part-time Associate Professor. His current research interests include the control of industrial motion systems with a special focus on nonlinear control, feedforward and learning control, and data-driven optimization and self-tuning. He was a recipient of the IEEE Control Systems Technology Award 2015 for variable gain control and its applications to wafer scanners. He is an Associate Editor of *IFAC Mechatronics*.

Authorized licensed use limited to: Eindhoven University of Technology. Downloaded on June 26,2023 at 08:45:42 UTC from IEEE Xplore. Restrictions apply.